Title

Joint eigenvector estimation from mutually anisotropic tensors improves susceptibility tensor imaging of the brain, kidney, and heart

Permalink

https://escholarship.org/uc/item/68z548fd

Journal

Magnetic Resonance in Medicine, 77(6)

ISSN

0740-3194

Authors

Dibb, Russell
Liu, Chunlei

Publication Date

2017-06-01

DOI

10.1002/mrm.26321

Peer reviewed

Joint Eigenvector Estimation from Mutually Anisotropic Tensors Improves Susceptibility Tensor Imaging of the Brain, Kidney, and Heart

Russell Dibb[1,2] and **Chunlei Liu**[1,2,3,4]

[1]Center for In Vivo Microscopy, Duke University Medical Center, Durham, NC, USA

[2]Biomedical Engineering, Duke University, Durham, NC, USA

[3]Brain Imaging & Analysis Center, Duke University Medical Center, Durham, NC, USA

[4]Radiology, Duke University Medical Center, Durham, NC, USA

Abstract

Purpose—To develop a susceptibility-based MRI technique for probing the microstructure and fiber architecture of magnetically anisotropic tissues—such as white matter of the central nervous system, renal tubules, and myocardial fibers—in 3D using susceptibility tensor imaging (STI) tools.

Theory—STI can probe tissue microstructure but is limited by reconstruction artifacts due to absent phase information outside the tissue and noise. We propose a strategy for improving STI accuracy through estimating a joint eigenvector from mutually anisotropic susceptibility and relaxation tensors.

Methods—Joint eigenvector estimation was validated using numerical phantom simulations. Gradient-recalled echo image data were acquired in multiple specimen orientations from the ex vivo mouse brain, kidney, and heart. Susceptibility tensor data were reconstructed using STI, regularized STI, and the proposed algorithm of mutually anisotropic and joint eigenvector STI (MAJESTI). Fiber map and tractography results from each technique were compared to diffusion tensor data.

Results—Phantom and specimen data show that MAJESTI improves the quality of susceptibility tensor reconstruction, particularly for the purposes of tissue orientation mapping and susceptibility-based fiber tractography.

Conclusion—MAJESTI shows promise as a method for improved susceptibility tensor estimation, more robust fiber mapping, and consistent tractography in the intact brain, kidney, and heart.

Keywords

Anisotropic magnetic susceptibility; Quantitative susceptibility mapping; Susceptibility tensor imaging; Resonance frequency shift

Correspondence: Chunlei Liu, PhD, Brain Imaging and Analysis Center, Duke University School of Medicine, 2424 Erwin Road, Suite 501, Campus Box 2737, Durham, NC 27705, USA, Fax: +1 919 681 7033, chunlei.liu@duke.edu.

INTRODUCTION

Magnetic resonance imaging (MRI) can be used to probe the microstructure of magnetically anisotropic tissues such as brain white matter (1–5), kidney (6), and heart (7). Understanding the mechanisms governing both isotropic and anisotropic susceptibility in these tissues may lead to improved techniques for assessing tissue structure, chemical composition, and viability. One such technique is susceptibility tensor imaging (STI) (8). STI takes advantage of gradient-recalled echo (GRE) phase information in order to reveal both the directionality and strength of the underlying tissue susceptibility anisotropy. This technique has been successfully applied as a preclinical imaging tool, particularly in magnetic resonance histology studies, where methods for imaging a specimen at multiple orientations have been developed (9). In this domain, the sensitivity of STI to the cellular content of tissues may be useful for observing structural and chemical alterations induced by diseases and disorders in the brain (8), kidney (10), and heart (7).

The structure and orientation of axon fiber bundles, renal tubules, and myocardial fibers play important roles in the function and health of the brain, kidney, and heart, respectively. Typically, preclinical structural fiber mapping is carried out through histological methods or diffusion tensor imaging (DTI), each having its respective advantages and disadvantages. For instance, histology provides extraordinary structural and chemical detail (11,12), but is labor-intensive and requires the destruction of the organ. High-resolution, preclinical DTI provides excellent structural information (13–21), but lacks sensitivity to chemical properties that are highlighted by other methods. On the other hand, susceptibility-based MRI yields nondestructive, 3D isotropic, high-resolution imaging that is sensitive to chemical composition *in addition* to structure (2,7,9). Based on our experience, however, we have found that STI reconstruction is vulnerable to noise and to low-frequency artifacts in reconstructed tensor images.

Sophisticated techniques, including regularization methods, have been proposed to improve susceptibility tensor estimation (5,22,23). Still, further improvements are needed for accurate, robust, and efficient tensor estimation and fiber tractography. Obtaining data at more specimen orientations improves reconstruction quality at the cost of additional scan time, and may have diminishing returns after exceeding the minimally required six orientations (22). Alternatively, the effective spin-spin relaxation rate (R_2*) may be simultaneously acquired with image phase using a multi-echo GRE pulse sequence. In addition to providing microstructural detail in high-field imaging (24), R_2* exhibits orientation dependence in magnetically anisotropic tissues such as white matter (25,26) and can be used to map fiber orientations (27–29).

Here, we propose an algorithm to improve susceptibility property maps of white matter fiber bundles, renal tubules, and myocardial fibers by incorporating information from both magnitude-derived relaxation and phase-derived susceptibility tensors. Specifically, we estimate a joint eigenvector system of the two tensors. The method is first tested on a numerical phantom to validate its effectiveness in mitigating image artifacts that appear in tensor orientation maps reconstructed with STI. The technique is then applied to intact

mouse brain, kidney, and heart. The resulting fiber tracts are compared to DTI-based fiber orientation maps. In addition to improving susceptibility-based tractography of white matter fibers and renal tubules, joint eigenvector estimation has allowed us to perform STI fiber tracking of a whole heart successfully for the first time (30).

THEORY

Reconstruction of Second-Order Relaxation and Susceptibility Tensors

Anisotropic tissue relaxation may be represented by a second-order tensor (see Supporting Information). In relaxation tensor imaging (RTI), a symmetric 3×3 relaxation tensor, $\mathbf{R}$, is derived from the effective R_2^* values acquired at multiple orientations ($i = 1, 2, \ldots n$) following

$$r_2^{*(i)}(\mathbf{r}) = \hat{\mathbf{h}}^{(i)^{\mathbf{T}}} \mathbf{R}(\mathbf{r}) \hat{\mathbf{h}}^{(i)} \quad [1]$$

$r_2^{*(i)}(\mathbf{r})$ and $\hat{\mathbf{h}}^{(i)}$ represent the observed relaxation rate and the unit vector of the applied magnetic field, respectively, for the ith orientation, $\mathbf{r}$ is the spatial position vector, and $\mathbf{T}$ is the transpose operation. Since $\mathbf{R}$ is symmetric, these n equations can be rewritten as one equation in terms of the six independent elements of the tensor,

$$\mathbf{H}[\ R_{11}(\mathbf{r})\ \ R_{12}(\mathbf{r})\ \ R_{13}(\mathbf{r})\ \ R_{22}(\mathbf{r})\ \ R_{23}(\mathbf{r})\ \ R_{33}(\mathbf{r})\ ]^{\mathbf{T}} = r_2^*(\mathbf{r}) \quad [2]$$

$\mathbf{H}$ is an $n{\times}6$ system matrix populated with the magnetic field orientation information,

$$\mathbf{H} = \begin{bmatrix} \hat{h}_1^{(1)}\hat{h}_1^{(1)} & 2\hat{h}_1^{(1)}\hat{h}_2^{(1)} & 2\hat{h}_1^{(1)}\hat{h}_3^{(1)} & \hat{h}_2^{(1)}\hat{h}_2^{(1)} & 2\hat{h}_2^{(1)}\hat{h}_3^{(1)} & \hat{h}_3^{(1)}\hat{h}_3^{(1)} \\ \hat{h}_1^{(2)}\hat{h}_1^{(2)} & 2\hat{h}_1^{(2)}\hat{h}_2^{(2)} & 2\hat{h}_1^{(2)}\hat{h}_3^{(2)} & \hat{h}_2^{(2)}\hat{h}_2^{(2)} & 2\hat{h}_2^{(2)}\hat{h}_3^{(2)} & \hat{h}_3^{(2)}\hat{h}_3^{(2)} \\ \vdots & \vdots & \vdots & \vdots & \vdots & \vdots \\ \hat{h}_1^{(n)}\hat{h}_1^{(n)} & 2\hat{h}_1^{(n)}\hat{h}_2^{(n)} & 2\hat{h}_1^{(n)}\hat{h}_3^{(n)} & \hat{h}_2^{(n)}\hat{h}_2^{(n)} & 2\hat{h}_2^{(n)}\hat{h}_3^{(n)} & \hat{h}_3^{(n)}\hat{h}_3^{(n)} \end{bmatrix} \quad [3]$$

In STI, tissue susceptibility is similarly described by a tensor. Normalized phase data in the k-space, $\tilde{\theta}\mathbf{k}$, are related to the magnetic susceptibility distribution (8),

$$\tilde{\theta}(\mathbf{k}) = \frac{\Delta f(\mathbf{k})}{\bar{\gamma} h_0 \mu_0} = \frac{1}{3}\hat{\mathbf{h}}^{\mathbf{T}}\chi(\mathbf{k})\hat{\mathbf{h}} - \mathbf{k}^{\mathbf{T}}\hat{\mathbf{h}}\frac{\mathbf{k}^{\mathbf{T}}\chi(\mathbf{k})\hat{\mathbf{h}}}{\mathbf{k}^{\mathbf{T}}\mathbf{k}} \quad [4]$$

Here, $f(\mathbf{k})$ is the frequency shift (referenced to the Larmor frequency) transformed into k-space, $\bar{\gamma}$ is the gyromagnetic ratio for water proton, h_0 is the amplitude of the applied magnetic field, μ_0 is the permittivity of free space, $\chi(\mathbf{k})$ is the second-order susceptibility

tensor in the frequency domain, and **k** is the spatial frequency vector. This relationship is rewritten in terms of the six independent elements of the symmetric susceptibility tensor, $\boldsymbol{\chi}(\mathbf{k})$,

$$\mathbf{A}\begin{bmatrix} \chi_{11}(\mathbf{k}) & \chi_{12}(\mathbf{k}) & \chi_{13}(\mathbf{k}) & \chi_{22}(\mathbf{k}) & \chi_{23}(\mathbf{k}) & \chi_{33}(\mathbf{k}) \end{bmatrix}^{\mathrm{T}} = \tilde{\boldsymbol{\theta}}(\mathbf{k}) \quad [5]$$

The system matrix, **A**, is fully detailed by Liu (8). One way to invert Eqs. [2] and [5] is using least-squares estimation which may be augmented by regularization terms to reduce error due to imperfect registration and random noise (23) and suppress anisotropy in tissue regions where susceptibility and relaxation are expected to be predominantly isotropic (22) (see Supporting Information).

Joint Estimation of Susceptibility-based Tensors

Susceptibility and relaxation tensor data can be combined to effectively correct errors in tensor orientation. The R_2^* relaxation rate of a set of parallel cylinders is positively correlated with the magnetic susceptibility difference between the objects and the surrounding medium (31). In magnetically anisotropic tissues, the orientation dependence of susceptibility contributes to the orientation dependence of R_2^*. For instance, white matter fiber bundles oriented perpendicular to the field direction have both larger susceptibility differences with the surrounding tissue and larger R_2^* than when the fiber bundles are parallel (25,26). This is commonly attributed to the susceptibility anisotropy of myelin (3,4,32). Similar orientation dependence is observed in myofibers, which can be ascribed to the susceptibility anisotropy of α-helix proteins in muscle tissue (7,33,34). Susceptibility anisotropy is also present in the kidney, and it has been suggested that the numerous infoldings of the lipid bilayer membranes of renal transporting epithelia produce the largest magnetic susceptibility differences when the tubular structure of the nephron is parallel to the applied magnetic field (9).

A key difference between susceptibility and relaxation tensors is that for white matter bundles and myofibers, the fiber axis is represented by the *major* eigenvector of the susceptibility tensor and the *minor* eigenvector of the relaxation tensor. This is because when the white matter fiber bundle or myofiber is parallel to the applied field, the susceptibility is the largest (i.e. most paramagnetic) (7,8) while relaxation is the smallest (27,29). For the nephron, the opposite is true—the tubule direction is indicated by the minor eigenvector of the susceptibility tensor (9). A second source of relaxation anisotropy may be superposed on the inherent relaxation anisotropy of these tissues by using contrast agents, as shown in myocardium (29). Contrast agents create strong, heterogeneous fields localized around capillary vessels (29). Brownian motion of proton spins through these fields increases R_2 dependent on the orientation of the vessel (35,36). This results in the *minor* eigenvector of the relaxation tensor indicating the orientation of the capillaries (29). This signifies the approximate direction of the underlying tissue structure, since blood vessels preferentially orient parallel to axon fibers in white matter (37), the vasa recta capillaries align with the

long loop of Henle in the nephron (38), and capillaries in the heart run parallel to myofibers (39).

Establishing the constraint that the relaxation and susceptibility tensors share an eigenvector that corresponds to the fiber direction could, theoretically, improve the accuracy of STI fiber mapping and tractography. Though we have explored several ways to apply this constraint, one method stood out as being both effective and efficient. It begins by calculating the joint eigenvectors of a weighted combination of χ and $\mathbf{R}$ through eigen decomposition:

$$\nu\chi - \mathbf{R} = \mathbf{Q}(\nu\Lambda_\chi - \Lambda_R)\mathbf{Q}^T \quad [6]$$

Here, ν makes the units of χ and $\mathbf{R}$ consistent and on a similar scale in order to facilitate balanced joint eigenvector estimation, with $|\nu|$ on the order of 1×10^8 Hz. Each column of $\mathbf{Q}$ is a shared eigenvector of $-\mathbf{R}$ and $\nu\chi$, and Λ_χ and Λ_R are diagonal matrices of the eigenvalues of χ and $\mathbf{R}$, respectively. Relaxation is defined as $-\mathbf{R}$, and the sign of ν is selected to ensure that the diagonal entries of $\nu\Lambda_\chi$ and $-\Lambda_R$ are ordered from most positive to least positive. This way, the major eigenvector of $\mathbf{Q}$ aligns with the tissue structure orientation. This eigenvector can equivalently point in equal and opposite directions.

The susceptibility eigenvalues are further estimated in the frame of reference of the joint eigenvectors, $\mathbf{Q}$. A 6×3 matrix, $\mathbf{V}$, which is defined from the entries of $\mathbf{Q}$ as follows:

$$\mathbf{V} = \begin{bmatrix} Q_{11}^2 & Q_{12}^2 & Q_{13}^2 \\ Q_{11}Q_{21} & Q_{12}Q_{22} & Q_{13}Q_{23} \\ Q_{11}Q_{31} & Q_{12}Q_{32} & Q_{13}Q_{33} \\ Q_{21}^2 & Q_{22}^2 & Q_{23}^2 \\ Q_{21}Q_{31} & Q_{22}Q_{32} & Q_{23}Q_{33} \\ Q_{31}^2 & Q_{32}^2 & Q_{33}^2 \end{bmatrix} \quad [7]$$

The diagonal entries of Λ_χ are estimated by inverting a modified version of Eq. [5] using the known eigenvector terms in $\mathbf{V}$:

$$\mathbf{A}\mathrm{FT}\{\mathbf{V}[\begin{array}{ccc} \Lambda_{\chi_1} & \Lambda_{\chi_2} & \Lambda_{\chi_3} \end{array}]^T\} = \tilde{\boldsymbol{\theta}}(\mathbf{k}) \quad [8]$$

Here, FT denotes the Fourier transform. The algorithm, mutually anisotropic and joint eigenvector susceptibility tensor imaging (MAJESTI), is summarized in Fig. 1.

METHODS

Numerical Simulations

To validate MAJESTI, a 3D 64×64×64 numerical phantom was created with each voxel represented by cylindrically symmetric susceptibility and R_2* tensors. These tensors have common eigenvectors that vary gradually in orientation for both the horizontal and vertical directions. The tensor orientations in the lower portion of the phantom were patterned after

the heart wall, and the upper portion contains three uniformly anisotropic tensor regions, represented in the phantom by red, green, and blue cylinders with the color representing eigenvector orientations (Fig. 2A). R_2^* and frequency shift maps were calculated from the tensor-valued data using Eqs. [1] and [4], respectively. This was done for 12 magnetic field orientations (Fig. 2B), each having one of six uniformly distributed azimuth angles (0°, 60°, 120°, 180°, 240°, and 300°) and one of two zeniths (35° and 70°). R_2^* error due to bulk inhomogeneity effects was simulated as $\gamma \Delta B/2$, where ΔB is the full width at half maximum of field inhomogeneity within a voxel. ΔB was generated from smoothly varying field effects in the range of −0.1 to 0.1 ppm to mimic field inhomogeneity in the narrow field of view of the specimen scans. Complex-valued, multi-echo image data were then generated according to

$$S = S_0 e^{-j2\pi \Delta f TE} e^{-R_2^* TE} \quad [9]$$

where, for each individual echo and orientation, S is the complex-valued image array, S_0 is the initial signal magnitude (referred to as $S_{0,int}$ and $S_{0,ext}$ to distinguish between the interior and the exterior of the phantom, respectively), j is the unit imaginary number, Δf is the frequency shift map, and TE is the echo time ($TE_1/\Delta TE/TE_8 = 3.0/5.5/41.5$ ms). The images were then transformed into k-space, where Gaussian noise was added to the real and imaginary data separately to yield a magnitude image signal-to-noise ratio (SNR) of 30 at TE = 0 ms. After the data were transformed back into the image domain, R_2^* maps were recalculated from the noisy magnitude data using a log-transformed linear regression model with SNR weighting. The multi-echo phase data were unwrapped using a Laplacian operator (40), normalized by TE, and then combined into a single frequency map using R_2^*-weighted averaging to improve SNR (41). Regularized RTI using Eq. [2] augmented with Supporting Eqs. [S1–S4] was performed on the R_2^* data before and after introducing bulk inhomogeneity and noise. STI data were reconstructed with $S_{0,ext} = 1$ and no noise, with $S_{0,ext} = 0$ and no noise, and with $S_{0,ext} = 0$ and noise. Regularized STI (rSTI) using Eq. [5] augmented with Supporting Eqs. [S1–S4] was then performed on the phase data with $S_{0,ext} = 0$, both with and without noise. The rSTI results should be similar to those achieved by Li et al. using mean magnetic susceptibility regularized STI (42). For each set of simulated data, the results of the regularized RTI and rSTI reconstructions were then used to estimate a joint eigenvector system using the proposed MAJESTI reconstruction algorithm (Fig. 1).

The mean susceptibility and susceptibility anisotropy were calculated as $\bar{\chi} = \text{tr}(\boldsymbol{\chi})/3$ and $\Delta\chi = \chi_1 - (\chi_2 + \chi_3)/2$, where $\chi_{1,2,3}$ are the primary, secondary, and tertiary susceptibility eigenvalues. For the simulated data, a voxelwise calculation of percent error was used to determine bias in the reconstructed $\bar{\chi}$ and $\Delta\chi$ following

$$E_{\hat{y}} = \frac{\hat{y} - y}{|y|} \times 100 \quad [10]$$

where $E_{\hat{y}}$ is percent error, and y and $\hat{y}$ are the true and reconstructed values, respectively. The angular difference between the reconstructed primary eigenvector ($\hat{\mathbf{u}}_{\chi,1}$) and the true eigenvector ($\hat{\mathbf{u}}_{t,1}$) was measured with the two spherical coordinate angles (φ_1, φ_2) in the coordinate system of ($\hat{\mathbf{u}}_{t,1}$, $\hat{\mathbf{u}}_{t,2}$, $\hat{\mathbf{u}}_{t,3}$). Tensor error measurements were calculated only within the voxels defined by the anisotropic tissue region (M) to emphasize the effect of each reconstruction algorithm in this region.

Animal Models

All animal studies were approved by the Duke University Institutional Animal Care and Use Committee. Only adult C57BL/6 mice (Charles River Labs, Durham, NC) were used for this study.

Brain Specimen—An 18-month-old, female mouse was anesthetized with Nembutal (Lundbeck Inc. Deerfield, IL, USA) and transcardially perfused with a peristaltic pump first with 0.9% saline and then 50 mM of Gd-HP-DO3A (ProHance; Bracco Diagnostics, Monroe Township, NJ) in 10% buffered formalin (Buffered Formalde-Fresh; Fisher Scientific, Hampton, NH) according to the "active staining" procedure detailed by Johnson et al. (43). The head was removed with the brain intact and immersed in 10% buffered formalin overnight. The specimen was then stored in 2.5 mM Gd-HP-DO3A in 10 mM phosphate-buffered saline (PH 7.4, SIGMA P-3813).

Kidney Specimens—Four 15-week-old, male mice were anesthetized with isoflurane, a midline abdominal incision was made, and a catheter was inserted into the heart for transcardial perfusion fixation. As described in (9), each animal was perfused with saline and 0.1% heparin (1,000 USP units/ml, SAGENT Pharmaceuticals, Schaumburg, IL) followed by 10% formalin, each at 8 ml/min for 5 minutes. The kidney from each mouse was excised, immersed in 10% formalin overnight, and later stored in a solution of 2.5 mM Gd-HP-DO3A in 10 mM phosphate-buffered saline.

Heart Specimen—An 18-week-old, male mouse was anesthetized with Nembutal. A catheter was inserted into the jugular vein, and the animal was perfused by a peristaltic pump with 0.2% heparin in 0.9% saline solution at a rate of 8 ml/min for 5 minutes to flush out the blood (44). The tissue was perfusion-fixed using a 150 ml solution of 50 mM Gd-HP-DO3A in 10% buffered formalin at a rate of 8 ml/min. Finally, to preserve the shape of the heart, the specimen was perfused with a heated 1.3% liquid agarose gel (SIGMA A9414-25G) solution at a rate of 8 ml/min for 2.5 minutes. After the gel cooled, the heart was excised and stored for three days in a solution of 2.5 mM Gd-HP-DO3A in 10 mM phosphate-buffered saline.

MR Microscopy—Each specimen was firmly secured in an acrylic specimen cartridge and immersed in Galden (Solvay Specialty Polymers, Alpharetta, GA, USA) to limit susceptibility artifacts at the tissue boundary and provide a dark background in the images. The cartridge was placed inside a sphere, allowing for an arbitrary specimen orientation inside the coil. The brain specimen was positioned in a quadrature volume coil with a 32-mm internal diameter (m2m Imaging, Cleveland, OH) for data acquisition using a 7.0 T,

210-mm horizontal bore Magnex magnet. The coil apparatus (9) for the heart and kidney specimens supported a solenoid RF resonator (21-mm diameter, 21-mm length) for data acquisition using a 9.4 T, 89-mm vertical bore Oxford magnet. Each magnet was controlled by an Agilent VnmrJ 4.0 console. The scan protocols and their respective parameters are listed in Table 1. Prior to every multiple-gradient-recalled echo (MGRE) image acquisition, the specimen was manually repositioned in a new orientation with respect to the magnetic field. Each orientation approximated one of the simulated phantom orientations described earlier, and the exact orientations were later determined using registration. After STI acquisition, the specimen cartridge was next placed inside a smaller RF resonator (14-mm diameter; 21-mm length). DTI data were then acquired with a 3D spin-echo sequence with monopolar, half-sine-shaped diffusion gradients: one image without diffusion weighting followed by twelve diffusion-weighted images with gradient orientations selected based on the electrostatic repulsion model (45).

MR Image Reconstruction and Analysis—Tissue masks were created from magnitude data to aid in phase processing. Additionally, regions of anisotropic susceptibility (M) were defined to include white matter tracts in the brain, all tissues excluding large vessels in the kidney, and myocardial tissue excluding large vessels in the heart. R_2* maps were calculated from the MGRE magnitude image data for each specimen orientation using a least-squares regression model with SNR weighting. The phase data of each individual echo image underwent unwrapping and background phase removal using iHARPERELLA in STI Suite (46). The frequency data from the multi-echo images were normalized by TE and then combined into a single frequency map using an R_2*-weighted average (41). The MGRE magnitude images were registered to the B_0 image of the DTI dataset using FSL (47). The corresponding affine image transformations were then applied to both the R_2* and processed frequency maps.

As described in the phantom simulation, relaxation tensor data were calculated using regularized RTI, and the susceptibility tensor data were calculated with STI, rSTI, and MAJESTI. MAJESTI's sensitivity to ν was determined by estimating joint eigenvectors using a range of values: $1\times10^4 < |\nu| < 1\times10^{12}$. Since data were acquired from only one brain and one heart specimen, sensitivity analyses were performed on data from these organ specimens i) as acquired, ii) with added noise to halve the image SNR, and iii) with the isotropic resolution decreased by a factor of two. Property maps for $\bar{\chi}$, $\tilde{\chi}$, and $\hat{\mathbf{u}}_{\chi,1}$ were calculated for each susceptibility tensor reconstruction as described previously. The spherical angles (φ_1, φ_2) between the primary susceptibility eigenvector and diffusion eigenvector were calculated in the anisotropic region (M). Eigenvector orientation comparisons to DTI in the kidney were limited to the inner medulla (IM) because diffusion tensor fractional anisotropy in the outer medulla (OM) and cortex (CO) is too low to provide reliable diffusion eigenvector data (9). The effect of each algorithm on tractography was analyzed using Diffusion Toolkit and TrackVis (48). The tractography was generated for voxels within the defined anisotropic region (M) using an angle threshold of 45°. All other simulations, image reconstructions, and analytical calculations were performed in MATLAB R2015b (MathWorks Inc., Natick, MA, USA).

RESULTS

Numerical Phantom Tensor Reconstruction

The STI results in Fig. 2 show that when the exterior phase information is present (i.e., $S_{0,ext}$ = 1) and noise is absent, the reconstructed susceptibility tensor data was almost identical to the original phantom data. χ was slightly underestimated in the red and green circles and overestimated in the blue circle (Fig. 2D, yellow single arrows), likely due to small errors in phase processing (see Supporting Information). When exterior phase information was absent (i.e., $S_{0,ext}$ = 0), reconstructed tensor errors were most visible near the phantom boundary in the $\hat{\mathbf{u}}_{\chi,1}$ and χ maps (Fig. 2C–D, yellow double arrows). This also shifted $\bar{\chi}$ to be more positive throughout the phantom and changed and the $\bar{\chi}$ contrast between different phantom regions (Fig. 2E). The absence of exterior phase resulted in median error measurements of E_χ = −34.5%, $E_{\bar{\chi}}$ = 85.5%, and φ_1 = 12.3° (Fig. 3D–F). Following the addition of noise, these figures grew to −43.7%, 90.6%, and 15.9°, respectively (Fig. 3J–L). In the data simulated with noise, rSTI reduced the median φ_1 to 15.2° (Fig. 3B,F), but introduced additional bias to χ (Fig. 3D, median E_χ of −52.2%). MAJESTI (using $\nu = 7\times10^8$) was most effective in correcting the voxels with large orientation error (yellow arrows in Fig. 3A,G) and produced median φ_1 values of 7.2° and 11.7° in the noiseless and noisy data, respectively (Fig. 3F,L). Increasing the relative weight of $\mathbf{R}$ using smaller values of ν improved the accuracy of the joint eigenvector when the simulated bulk inhomogeneity artifacts were minor. Decreasing the relative weight of $\mathbf{R}$ by using larger values of ν improved accuracy when these artifacts were major. Although the recalculated susceptibility eigenvalues from MAJESTI still underestimated the true anisotropy (Fig. 3J; median E_χ of −37.4% without noise, −52.1% with noise), the jointly estimated eigenvectors were a substantial improvement compared to the STI and rSTI reconstructions of the noisy phase data.

MAJESTI of the Brain

The STI, rSTI, and MAJESTI results in the mouse brain are shown in Fig. 4. STI produced the largest fiber orientation differences with DTI (median φ_1 = 47.4°). rSTI and MAJESTI decreased the median φ_1 to 36.4° and 30.4°, respectively. The improvement was seen throughout the anisotropic region (*M*), but was most noticeable in the corpus callosum (CC) and hippocampal commissure (HC, yellow arrows, Fig. 4C). The $\bar{\chi}$ map (Fig. 4D) was virtually unaffected by the choice of reconstruction algorithm. Regarding anisotropy, MAJESTI resulted in lower median χ (69.3 pbb) than STI (107.5 ppb) but higher than rSTI (59.1 ppb). Based on these values and the median E_χ values from the simulated STI reconstructions (Fig. 3G), a better range for the true median χ is approximately 120–190 ppb. This agrees somewhat with a QSM-based calculation of mean χ in Gd-enhanced white matter (approximately 140 ± 20 pbb) from a mouse brain specimen prepared using the same protocol (49). The sensitivity analysis found that the median φ_1 was smallest when ν = ~4×10^8, and was consistent within 1° for the image resolutions and SNRs tested when $4\times10^8 < \nu < 6\times10^8$ (Fig. 4H). The corrected fiber angles from the MAJESTI tensor data yielded modest improvements to the white matter fiber bundle tractography in the mouse brain. Fig. 5 shows that MAJESTI more thoroughly tracked fibers in the CC, HC, and anterior commissure (orange arrows); corrected the orientation of tracts in the CC (white arrows) and

HC (yellow arrows); and better delineated the cingulum (yellow double arrowheads) and the genu of the CC (white double arrowheads).

MAJESTI in the Kidney

Fig. 6 shows the STI, rSTI, and MAJESTI results from one representative kidney specimen. Fig. 6C shows that tensor orientation differences between STI and DTI in the IM are actually quite large for STI (median $\varphi_1 = 50.6 \pm 2.1°$) and, surprisingly, worse for rSTI ($55.1 \pm 2.7°$). MAJESTI drops the median φ_1 to $30.4 \pm 7.6°$, which can be attributed to the similar eigenvector orientations of the RTI and DTI data in the IM. Compared to STI, both rSTI and MAJESTI reduced the median χ in the IM from 74.9 ± 10.1 to 41.7 ± 5.2 and 25.4 ± 3.7 ppb, respectively. Anisotropy was approximately 40% lower in the OM and CO. Based on the errors values from simulation, the data suggest a true median χ of approximately 50–130 ppb in the Gd-enhanced renal tissue of the IM. The sensitivity analysis found that the median φ_1 was both smallest and consistent within 1° for all four kidney specimens when $\nu < {\sim}4 \times 10^7$ (Fig. 4H). Thus, the optimal joint eigenvector estimate in the Gd-enhanced renal tissue relied almost entirely on the relaxation tensor orientation. As in the brain specimen data, the $\bar{\chi}$ distributions (Fig. 6D) from each reconstruction were visually indistinguishable. Fig. 7 shows the STI, MAJESTI, and DTI tractography in the IM and OM of the kidney. Even in the highly anisotropic IM, STI tracts exhibited large differences with DTI. MAJESTI improved tractography congruity (white arrows, Fig. 7) and continuity (orange arrows, Fig. 7) to better resemble DTI.

MAJESTI in the Heart

Fig. 8 shows the STI, rSTI, and MAJESTI results for the heart specimen data. Analogous to the simulated phantom data, the reconstructed myofiber orientations are strongly affected in the boundary regions between the specimen and the exterior (Fig. 8A). Agreement between the primary STI and DTI eigenvectors is limited to the interventricular septum (IVS) (Fig. 8C, yellow double arrow). Regularization and joint eigenvector estimation reduced these artifacts, diminishing the median φ_1 from 45.4° in STI to 37.5° in rSTI and 25.0° in MAJESTI (Fig. 8E). These improvements are evident throughout the organ (Fig. 8C, yellow single arrows). Fig. 8G shows that MAJESTI produced a smaller median χ (32.9 ppb) than STI (54.6 ppb) and rSTI (38.5 ppb). Using the simulation error values as a guide, these calculations suggest a true median χ of approximately 70–100 pbb in the Gd-enhanced myocardial tissue. The sensitivity analysis found that the median φ_1 was smallest when $\nu = {\sim}2 \times 10^8$, and was consistent within 1° for the image resolutions and SNRs tested when $1 \times 10^8 < \nu < 5 \times 10^8$ (Fig. 8H). MAJESTI markedly enhanced susceptibility-based tractography in the heart relative to rSTI. Improvements included more continuous fiber tracts in the RVW (orange arrows; Fig. 9A–B, D–E), and tract orientations in the epicardial (white arrows, Fig. 9A–F) and endocardial (yellow arrows, Fig. 9A–F) regions of the left ventricle that closely resembled DTI. The tensor glyph maps show how MAJESTI produced smoothly transitioning tensor orientations in the LVW (Fig. 9G–I) by improving the fiber eigenvector orientation while only slightly reducing anisotropy.

DISCUSSION

Regularization improves susceptibility tensor orientation accuracy, and MAJESTI goes a step further by incorporating mutual eigenvector information in order to mitigate susceptibility tensor reconstruction artifacts. MAJESTI is more robust than our previous algorithm, conjoint relaxation and susceptibility tensor imaging (30), for estimating the complete susceptibility tensor because it calculates susceptibility eigenvalues using the original multi-orientation frequency image data (Eq. [8]). As a result, MAJESTI calculates $\bar{\chi}$ maps that are nearly identical to STI and rSTI (Fig. 3I,K), though χ is still underestimated. This is because the eigenvalues describe the degree to which a unit sphere either stretches or shrinks in the direction of the corresponding eigenvectors. If the eigenvectors are changed to better describe the tissue structure, the eigenvalues will change in order to fit the acquired data. This tradeoff between reconstructing a tensor image that has desired characteristics and one that fits the data is inherent in STI regularization in general.

MAJESTI's sensitivity to the selected ν value was demonstrated in Figs. 4H, 6H, and 8H. These analyses give the optimal value and range for ν for the Gd-enhanced organs, SNR values, and image resolutions tested. They also suggest that image SNR has a greater impact on RTI than STI, but that RTI greatly outperforms STI in resembling DTI eigenvector orientations in Gd-enhanced renal tissue. Contrarily, RTI and STI reconstruction quality are more comparable in the brain and heart, which leads to synergistic joint eigenvector estimates in these two organs (Figs. 4H and 8H).

Sources of Error

The most significant source of error in STI reconstruction spawns from incomplete and/or incorrect phase information (Fig. 2). Even though STI produces a very good fit to the available phase data from each specimen—forward calculations of image frequency from the reconstructed STI tensor generally yielded less than 10% error—the phantom simulation shows that STI reconstruction without external phase information results in overestimated $\bar{\chi}$, underestimated χ, and increased φ_1. A potential solution for absent exterior phase is to embed tissue specimens in agarose gel or another susceptibility-matched medium prior to scanning in order to preserve phase information outside the specimen. This, of course, would not be suitable for in vivo studies or even for many ex vivo studies. Alternatively, MAJESTI attempts to compensate for the lost phase information by integrating relaxation tensor data into the STI reconstruction. STI errors may also result from phase processing (see Supporting Information).

MAJESTI Tractography

MAJESTI successfully enhanced the continuity and conformity of susceptibility-based tractography (Figs. 5, 7, and 9). Despite these improvements, the MAJESTI results still show substantial differences between susceptibility- and diffusion-based tractography. This may be indicative of the different structural and chemical mechanisms underlying anisotropic susceptibility and diffusion tensors. In the heart, for example, the primary eigenvector of the diffusion tensor indicates the myofiber orientation, whereas the fiber sheet structure of the heart dictates that the secondary and tertiary eigenvectors consistently point

in the transmural direction and in a direction parallel to the epicardial tangent plane, respectively (79). The fiber sheet structure may have a much different influence over the primary, secondary, and tertiary susceptibility eigenvectors. Furthermore, the influence of myofilament proteins, collagen, and lipids may play a more prominent role in determining the tissue susceptibility tensor due to the chemical sensitivity of susceptibility imaging. In the brain, different cell types and organizations may likewise lead to dissimilar susceptibility and diffusion tensors. Additional work is necessary to uncover the roles that tissue geometry, organization, and composition play in influencing the susceptibility tensor and susceptibility-based tractography.

Limitations and Future Directions

Though MAJESTI is a significant step towards the robust estimation of tensor-valued susceptibility in the brain, kidney, and heart, the technique would benefit from further development. Ideally, MAJESTI would solve for $\mathbf{Q}$ and $\mathbf{\Lambda_\chi}$ simultaneously. This is difficult due to the nonlinear nature of applying an image-domain eigenvector constraint on the frequency-domain relationship between phase and susceptibility (Eq. [5]). An iterative solver that updates eigenvectors while simultaneously solving for both susceptibility and relaxation tensors may potentially yield a more accurate solution. One limitation of this study is its small sample size, which diminishes the inference that can be made regarding MAJESTI. However, we consistently demonstrated improved fiber orientation and tractography with MAJESTI in multiple organs with varied degrees of image quality, which supports the efficacy of the algorithm. Lastly, STI is currently limited to preclinical research, and is most feasible ex vivo. Each specimen in the study was prepared with Gd, shortening the T_1 and T_2* relative to similarly prepared specimens and enhancing anisotropy (7,9,49). STI is also feasible without the use of contrast agents (8,9). The practical considerations of performing this technique are discussed in the Supporting Information.

CONCLUSIONS

STI is a tool for studying magnetic susceptibility anisotropy in the brain, kidney, and heart, although it is prone to artifacts spawning from incomplete and/or incorrect phase image data. These artifacts disguise the true susceptibility properties of tissues and limit susceptibility-based tractography, especially when compared to DTI. MAJESTI improves STI by taking advantage of the information shared by susceptibility and relaxation tensors, resulting in higher quality tensor orientation estimates and enhanced continuity and conformity of susceptibility-based fiber tracts.

Supplementary Material

Refer to Web version on PubMed Central for supplementary material.

Acknowledgments

References

1. Wharton S, Bowtell R. Effects of white matter microstructure on phase and susceptibility maps. Magnetic Resonance in Medicine. 2015; 73(3):1258–1269. [PubMed: 24619643]

2. Liu C, Li W, Johnson GA, Wu B. High-field (9. 4 T) MRI of brain dysmyelination by quantitative mapping of magnetic susceptibility. Neuroimage. 2011; 56(3):930–938. [PubMed: 21320606]

3. Lee J, Shmueli K, Fukunaga M, van Gelderen P, Merkle H, Silva AC, Duyn JH. Sensitivity of MRI resonance frequency to the orientation of brain tissue microstructure. Proc Natl Acad Sci USA. 2010

4. Li W, Wu B, Avram AV, Liu C. Magnetic susceptibility anisotropy of human brain in vivo and its molecular underpinnings. Neuroimage. 2012; 59(3):2088–2097. [PubMed: 22036681]

5. Wisnieff C, Liu T, Spincemaille P, Wang S, Zhou D, Wang Y. Magnetic susceptibility anisotropy: cylindrical symmetry from macroscopically ordered anisotropic molecules and accuracy of MRI measurements using few orientations. Neuroimage. 2013; 70:363–376. [PubMed: 23296181]

6. Xie L, Sparks MA, Li W, Qi Y, Liu C, Coffman TM, Johnson GA. Quantitative susceptibility mapping of kidney inflammation and fibrosis in type 1 angiotensin receptor-deficient mice. NMR Biomed. 2013; 26(12):1853–1863. [PubMed: 24154952]

7. Dibb R, Qi Y, Liu C. Magnetic susceptibility anisotropy of myocardium imaged by cardiovascular magnetic resonance reflects the anisotropy of myocardial filament alphahelix polypeptide bonds. Journal of Cardiovascular Magnetic Resonance. 2015; 17(1):60. [PubMed: 26177899]

8. Liu C. Susceptibility tensor imaging. Magn Reson Med. 2010; 63(6):1471–1477. [PubMed: 20512849]

9. Xie L, Dibb R, Cofer GP, Li W, Nicholls PJ, Johnson GA, Liu C. Susceptibility tensor imaging of the kidney and its microstructural underpinnings. Magn Reson Med. 2014; 73(3):1270–1281. [PubMed: 24700637]

10. Xie, L., Dibb, R., Gurley, SB., Liu, C., Johnson, GA. Susceptibility tensor imaging reveals reduced anisotropy in renal nephropathy. 2015. Proceedings of the 23nd Annual ISMRM; Toronto, Canada. p. 463

11. LeGrice IJ, Smaill BH, Chai LZ, Edgar SG, Gavin JB, Hunter PJ. Laminar structure of the heart: ventricular myocyte arrangement and connective tissue architecture in the dog. The American journal of physiology. 1995; 269(2 Pt 2):H571–582. [PubMed: 7653621]

12. Pope AJ, Sands GB, Smaill BH, LeGrice IJ. Three-dimensional transmural organization of perimysial collagen in the heart. American journal of physiology Heart and circulatory physiology. 2008; 295(3):H1243–h1252. [PubMed: 18641274]

13. Hsu, EW., Healy, LJ., Einstein, DR., Kuprat, AP. Imaging-Based Assessment and Modeling of the Structures of the Myocardium. In: Guccione, JM.Kassab, GS., Ratcliffe, MB., editors. Computational cardiovascular mechanics: modeling and applications in heart failure. New York, NY: Springer; 2010. p. 27

14. Hsu EW, Muzikant AL, Matulevicius SA, Penland RC, Henriquez CS. Magnetic resonance myocardial fiber-orientation mapping with direct histological correlation. The American journal of physiology. 1998; 274(5 Pt 2):H1627–1634. [PubMed: 9612373]

15. Scollan DF, Holmes A, Winslow R, Forder J. Histological validation of myocardial microstructure obtained from diffusion tensor magnetic resonance imaging. The American journal of physiology. 1998; 275(6 Pt 2):H2308–2318. [PubMed: 9843833]

16. Kung GL, Nguyen TC, Itoh A, Skare S, Ingels NB Jr, Miller DC, Ennis DB. The presence of two local myocardial sheet populations confirmed by diffusion tensor MRI and histological validation. J Magn Reson Imaging. 2011; 34(5):1080–1091. [PubMed: 21932362]

17. Cheung JS, Fan SJ, Chow AM, Zhang J, Man K, Wu EX. Diffusion tensor imaging of renal ischemia reperfusion injury in an experimental model. NMR Biomed. 2010; 23(5):496–502. [PubMed: 20175152]

18. Jiang Y, Johnson GA. Microscopic diffusion tensor imaging of the mouse brain. Neuroimage. 2010; 50(2):465–471. [PubMed: 20034583]

19. Mori S, Itoh R, Zhang J, Kaufmann WE, van Zijl PCM, Solaiyappan M, Yarowsky P. Diffusion tensor imaging of the developing mouse brain. Magnetic Resonance in Medicine. 2001; 46(1):18–23. [PubMed: 11443706]

20. Strijkers GJ, Bouts A, Blankesteijn WM, Peeters TH, Vilanova A, van Prooijen MC, Sanders HM, Heijman E, Nicolay K. Diffusion tensor imaging of left ventricular remodeling in response to myocardial infarction in the mouse. NMR Biomed. 2009; 22(2):182–190. [PubMed: 18780284]

21. Sosnovik DE, Mekkaoui C, Huang S, Chen HH, Dai G, Stoeck CT, Ngoy S, Guan J, Wang R, Kostis WJ, Jackowski MP, Wedeen VJ, Kozerke S, Liao R. Microstructural impact of ischemia and bone marrow-derived cell therapy revealed with diffusion tensor magnetic resonance imaging tractography of the heart in vivo. Circulation. 2014; 129(17):1731–1741. [PubMed: 24619466]

22. Li X, van Zijl PCM. Mean magnetic susceptibility regularized susceptibility tensor imaging (MMSR-STI) for estimating orientations of white matter fibers in human brain. Magnetic Resonance in Medicine. 2014 n/a-n/a.

23. Liu C, Li W, Wu B, Jiang Y, Johnson GA. 3D fiber tractography with susceptibility tensor imaging. Neuroimage. 2012; 59(2):1290–1298. [PubMed: 21867759]

24. Köhler S, Hiller K-H, Waller C, Jakob PM, Bauer WR, Haase A. Visualization of myocardial microstructure using high-resolution T2* imaging at high magnetic field. Magn Reson Med. 2003; 49(2):371–375. [PubMed: 12541258]

25. Cherubini A, Peran P, Hagberg GE, Varsi AE, Luccichenti G, Caltagirone C, Sabatini U, Spalletta G. Characterization of white matter fiber bundles with T2* relaxometry and diffusion tensor imaging. Magn Reson Med. 2009; 61(5):1066–1072. [PubMed: 19253372]

26. Bender B, Klose U. The in vivo influence of white matter fiber orientation towards B(0) on T2* in the human brain. NMR Biomed. 2010; 23(9):1071–1076. [PubMed: 20665897]

27. Lee J, van Gelderen P, Kuo LW, Merkle H, Silva AC, Duyn JH. T2*-based fiber orientation mapping. Neuroimage. 2011; 57(1):225–234. [PubMed: 21549203]

28. Wharton S, Bowtell R. Gradient echo based fiber orientation mapping using R2* and frequency difference measurements. Neuroimage. 2013; 83:1011–1023. [PubMed: 23906549]

29. Vignaud A, Rodriguez I, Ennis DB, DeSilva R, Kellman P, Taylor J, Bennett E, Wen H. Detection of myocardial capillary orientation with intravascular iron-oxide nanoparticles in spin-echo MRI. Magn Reson Med. 2006; 55(4):725–730. [PubMed: 16506158]

30. Dibb, R., Liu, C. Whole-heart myofiber tractography derived from conjoint relaxation and susceptibility tensor imaging. 2015. Proceedings of the 23nd Annual ISMRM; Toronto, Canada. p. 287

31. Yablonskiy DA, Haacke EM. Theory of NMR signal behavior in magnetically inhomogeneous tissues: the static dephasing regime. Magn Reson Med. 1994; 32(6):749–763. [PubMed: 7869897]

32. van Gelderen P, Mandelkow H, de Zwart JA, Duyn JH. A torque balance measurement of anisotropy of the magnetic susceptibility in white matter. Magn Reson Med. 2014

33. Arnold W, Steele R, Mueller H. On the magnetic asymmetry of muscle fibers. Proc Natl Acad Sci USA. 1958; 44(1):1–4. [PubMed: 16590140]

34. Worcester DL. Structural origins of diamagnetic anisotropy in proteins. Proc Natl Acad Sci USA. 1978; 75(11):5475–5477. [PubMed: 281695]

35. Brown, RW.Cheng, Y-CN.Haacke, EM.Thompson, MR., Venkatesan, R., editors. Magnetic Resonance Imaging: Physical Principles and Sequence Design. John Wiley & Sons Ltd; 2014. Magnetic Properties of Tissues; p. 739-777.

36. Kennan RP, Zhong J, Gore JC. Intravascular susceptibility contrast mechanisms in tissues. Magn Reson Med. 1994; 31(1):9–21. [PubMed: 8121277]

37. Cavaglia M, Dombrowski SM, Drazba J, Vasanji A, Bokesch PM, Janigro D. Regional variation in brain capillary density and vascular response to ischemia. Brain Research. 2001; 910(1–2):81–93. [PubMed: 11489257]

38. Hook, JB. Toxicology of the kidney. Raven Press; 1981.

39. Greenbaum RA, Ho SY, Gibson DG, Becker AE, Anderson RH. Left ventricular fibre architecture in man. British heart journal. 1981; 45(3):248–263. [PubMed: 7008815]

40. Schofield MA, Zhu Y. Fast phase unwrapping algorithm for interferometric applications. Optics letters. 2003; 28(14):1194–1196. [PubMed: 12885018]

41. Wu B, Li W, Avram AV, Gho SM, Liu C. Fast and tissue-optimized mapping of magnetic susceptibility and T2* with multi-echo and multi-shot spirals. Neuroimage. 2012; 59(1):297–305. [PubMed: 21784162]

42. Li X, van Zijl PCM. Mean magnetic susceptibility regularized susceptibility tensor imaging (MMSR-STI) for estimating orientations of white matter fibers in human brain. Magnetic Resonance in Medicine. 2014; 72(3):610–619. [PubMed: 24974830]

43. Johnson GA, Cofer GP, Gewalt SL, Hedlund LW. Morphologic phenotyping with MR microscopy: the visible mouse. Radiology. 2002; 222(3):789–793. [PubMed: 11867802]

44. Angeli S, Befera N, Peyrat J-M, Calabrese E, Johnson GA, Constantinides C. A high-resolution cardiovascular magnetic resonance diffusion tensor map from ex-vivo C57BL/6 murine hearts. J Cardiov Magn Reson. 2014; 16(1):77.

45. Jones DK, Horsfield MA, Simmons A. Optimal strategies for measuring diffusion in anisotropic systems by magnetic resonance imaging. Magn Reson Med. 1999; 42(3):515–525. [PubMed: 10467296]

46. Li W, Avram AV, Wu B, Xiao X, Liu C. Integrated Laplacian-based phase unwrapping and background phase removal for quantitative susceptibility mapping. NMR Biomed. 2014; 27(2): 219–227. [PubMed: 24357120]

47. Jenkinson M, Bannister P, Brady M, Smith S. Improved optimization for the robust and accurate linear registration and motion correction of brain images. Neuroimage. 2002; 17(2):825–841. [PubMed: 12377157]

48. Wang, R., Benner, T., Sorensen, AG., Weeden, VJ. Diffusion Toolkit: A Software Package for Diffusion Imaging Data Processing and Tractography 2007. Proceedings of the 15th Annual ISMRM; Berlin, Germany. p. 3720

49. Dibb R, Li W, Cofer G, Liu C. Microstructural origins of gadolinium-enhanced susceptibility contrast and anisotropy. Magn Reson Med. 2014; 72(6):1702–1711. [PubMed: 24443202]
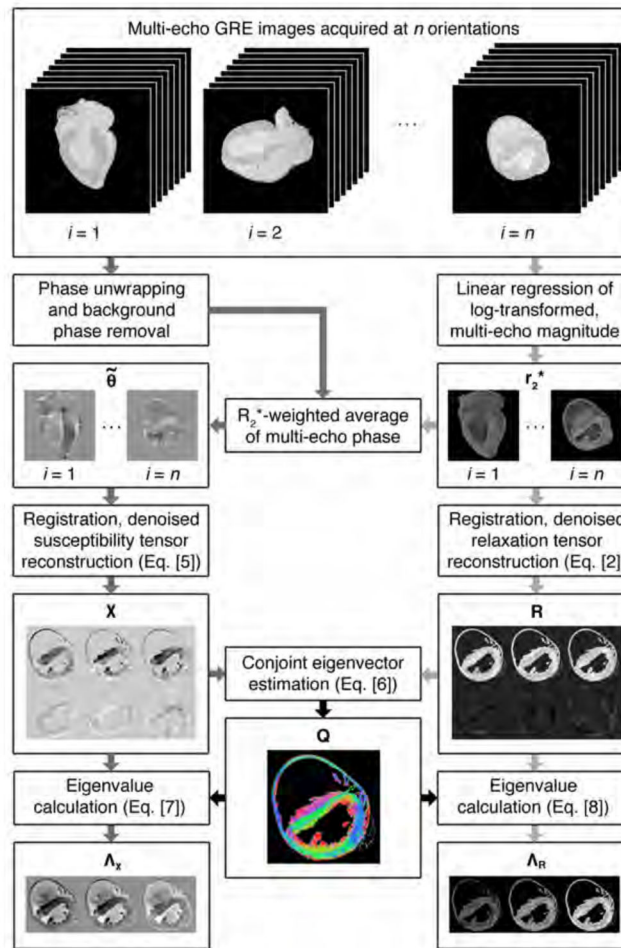
Fig. 1.
Algorithmic flow chart for mutually anisotropic and joint eigenvector susceptibility tensor imaging (MAJESTI). Multi-echo GRE image data are acquired and used to calculate normalized phase maps ($\tilde{\theta}$) and effective transverse relaxation maps (r_2^*) at n specimen orientations. Following registration, susceptibility (χ) and relaxation (R) tensor data is reconstructed using regularized STI and RTI. Weighted combination eigen decomposition of these tensors yields a system of joint eigenvectors (Q). Q and $\tilde{\theta}$ are used to calculate the susceptibility eigenvalues (Λ_χ).
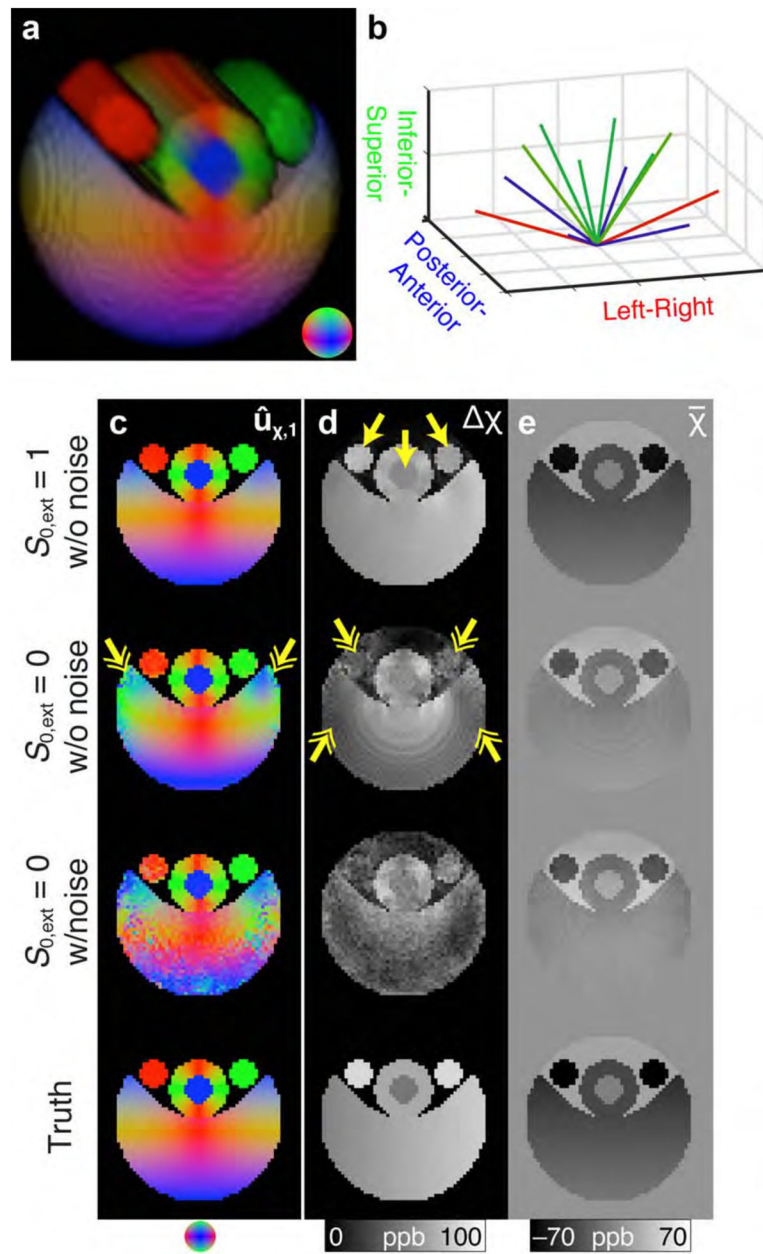
Fig. 2.
Phantom simulation results for STI reconstruction. Multi-echo GRE image data were simulated for a (A) spherical phantom at (B) 12 orientations relative to the magnetic field. (C) Susceptibility tensor orientation, (D) susceptibility anisotropy, and (E) mean susceptibility results were calculated for three simulation scenarios: with exterior phase information and without noise (first row), without exterior phase information and without noise (second row), and without exterior phase information and with noise (third row). The true tensor property maps are included for comparison (fourth row).
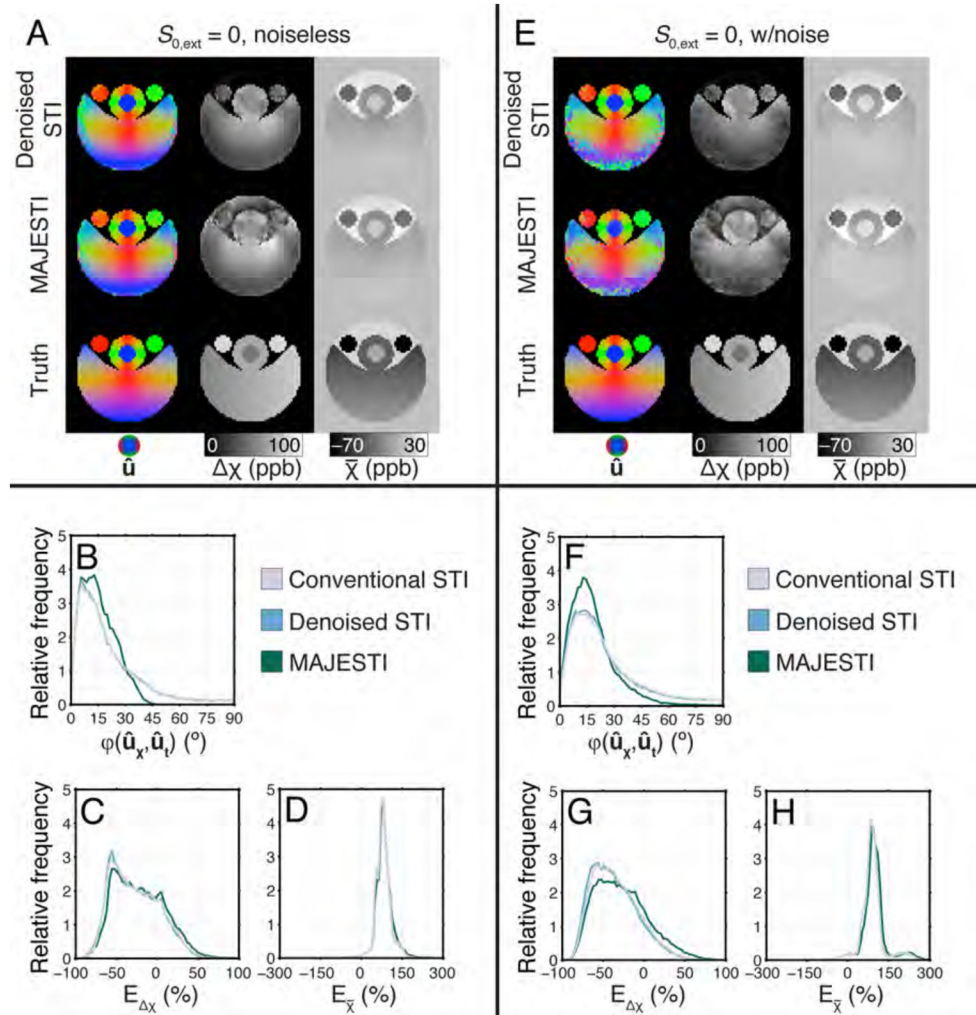
Fig. 3.
Phantom simulation results for the STI, rSTI, and MAJESTI reconstructions performed on the data without exterior phase information. Yellow arrows indicate reconstruction artifacts in (A) principal eigenvector maps. (B) Susceptibility anisotropy and (C) mean susceptibility maps from rSTI and MAJESTI show large differences compared to the truth. Histograms of (D) susceptibility anisotropy and (E) mean susceptibility error show that all three algorithms underestimate the true anisotropy and overestimate the true mean value. (F) Angular error histograms show the distribution of orientation differences between STI, rSTI, and MAJESTI eigenvectors and the ground truth using spherical coordinate angles (φ_1, φ_2). The addition of noise amplified artifacts in the (G) principal eigenvector, (H) susceptibility anisotropy and (I) mean susceptibility maps. Error histograms for (J) anisotropy and (K) mean susceptibility are similar to the case without noise. (F) Angular error histograms for each tensor reconstruction with noise show that MAJESTI yielded the smallest principal eigenvector orientation error.
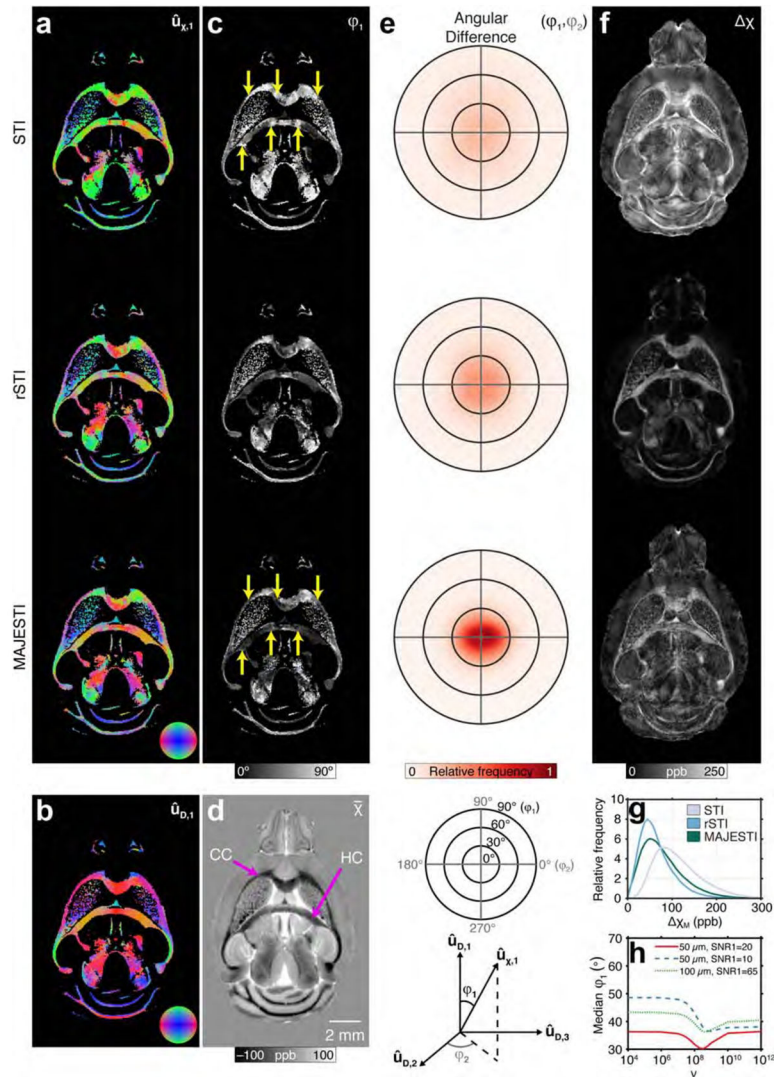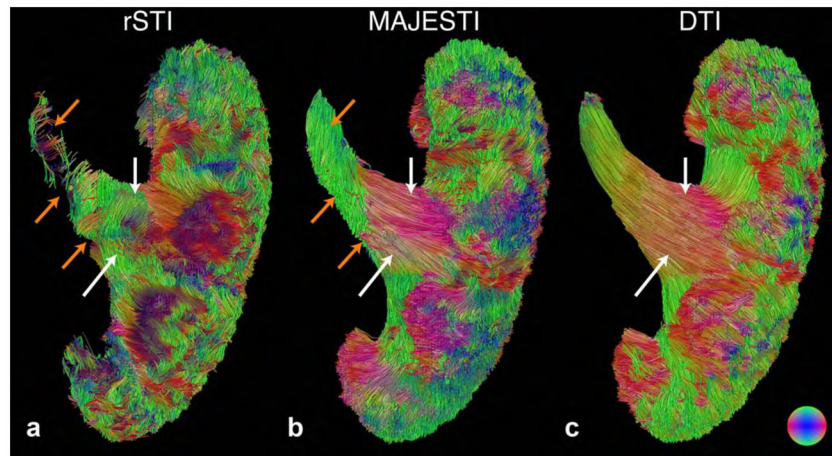
Fig. 4.
Susceptibility tensor reconstruction of the mouse brain using STI, rSTI, and MAJESTI. (A)
Principal eigenvector maps from each reconstruction algorithm are compared to (B) DTI in
the anisotropic region, *M.* (C) Angular error maps show MAJESTI's improvement over STI
(yellow arrows), particularly in the corpus callosum (CC) and hippocampal commissure
(HC)— structures that are delineated in (D) the mean susceptibility map. (E) Angular
difference histograms show that the MAJESTI principal eigenvectors were most similar to
DTI. (F) Susceptibility anisotropy maps for each reconstruction algorithm are quantitatively
represented in (G) histograms of susceptibility anisotropy in the anisotropic region, *M.* (H)
Sensitivity analysis showing the relationship between the median φ_1 and ν in original brain
data, the data with the SNR halved, and the data with reduced spatial resolution.
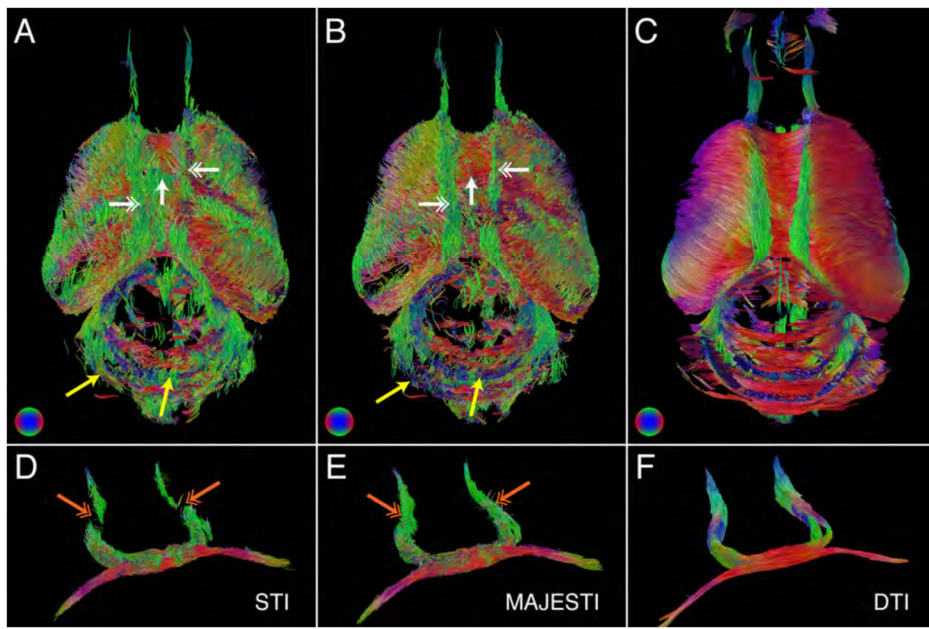
Fig. 5.
Susceptibility- and diffusion-based tractography in the mouse brain specimen. (A) Fiber tracts generated by rSTI were noisy and discontinuous. (B) MAJESTI tractography more closely resembled (C) DTI tractography in regions indicated by the white arrows. Compared to rSTI, MAJESTI better delineated the cingulum (yellow double arrowheads) and genu of the corpus callosum (yellow double arrowheads). (D), (E), and (F) show the tractography results in the hippocampal commissure and anterior commissure for the rSTI, MAJESTI, and DTI reconstructions, respectively. Yellow arrows indicate regions where MAJESTI more closely resembled DTI compared to rSTI. Orange arrows show regions where MAJESTI tracked fibers that rSTI did not. For clarity, only 20% of white matter fiber tracts longer that 1 mm are shown for the whole-brain tractography.
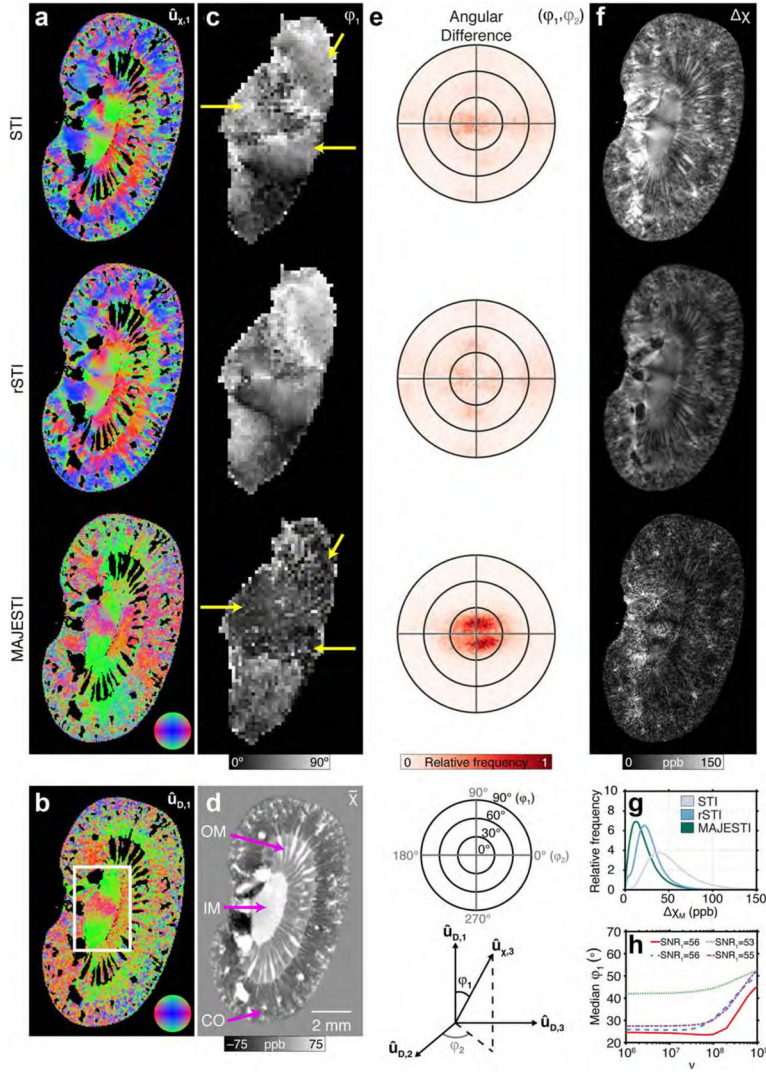
Fig. 6.
Susceptibility tensor reconstruction of a representative mouse kidney specimen using STI, rSTI, and MAJESTI. (A) Principal eigenvector maps from each reconstruction algorithm are compared to (B) DTI in the anisotropic region, *M*. (C) Angular error maps of the inner medulla (white rectangle in panel B) show MAJESTI's improvement over STI (yellow arrows). The inner medulla (IM), outer medulla (OM) and cortex (CO) of the kidney are delineated in (D) the mean susceptibility map. (E) Angular difference histograms show that the MAJESTI principal eigenvectors were most similar to DTI, while rSTI performed worse than STI. (F) Susceptibility anisotropy maps for each reconstruction algorithm are quantitatively represented in (G) histograms of susceptibility anisotropy in the anisotropic region, *M*. (H) Sensitivity analysis showing the relationship between the median φ_1 and ν in the four kidney specimens.

Fig. 7.
Susceptibility- and diffusion-based tractography in the mouse kidney specimen. (A) Fiber tracts generated by rSTI were discontinuous and incongruent to DTI. (B) MAJESTI tractography more closely resembled (C) DTI tractography in the inner medulla (white arrows). Orange arrows show regions where MAJESTI tracked fibers that rSTI did not. For clarity, only 50% of tubule tracts longer than 1 mm are shown.
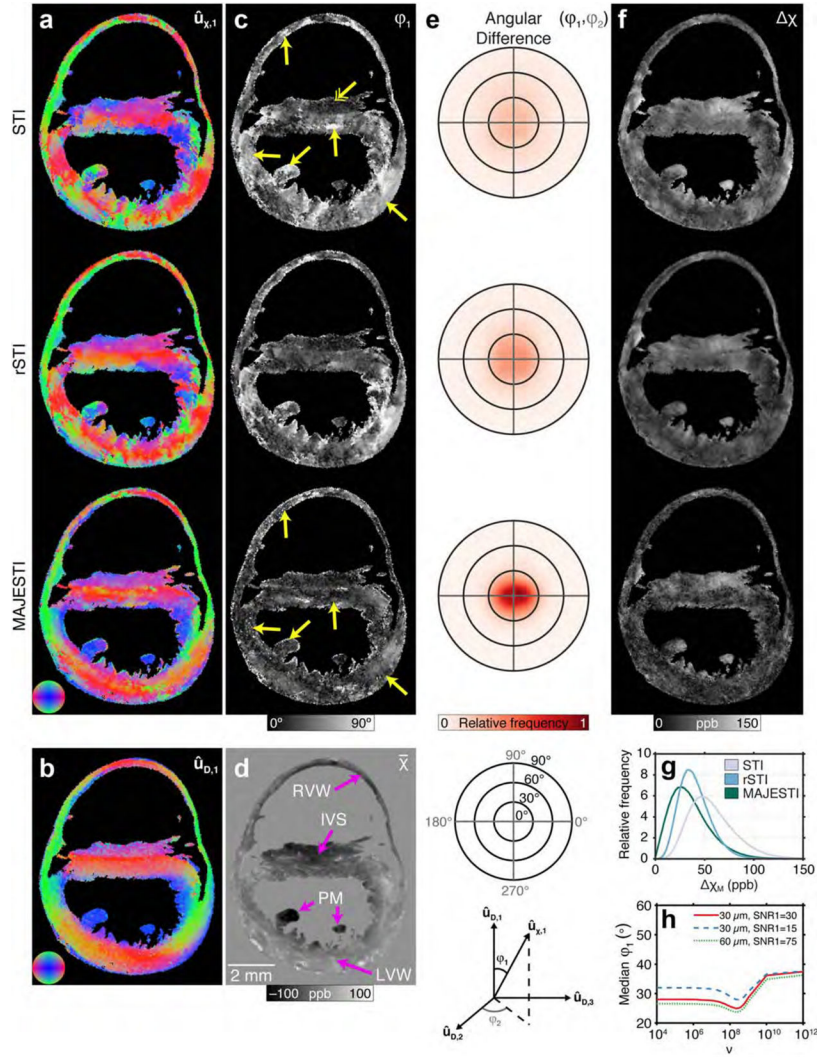
Fig. 8.
Susceptibility tensor reconstruction of the mouse heart using STI, rSTI, and MAJESTI. (A) Principal eigenvector maps from each reconstruction algorithm are compared to (B) DTI in the anisotropic region, *M*. (C) Angular error maps show MAJESTI's improvement over STI throughout the heart (yellow arrows). The right ventricle wall (RVW), interventricular septum (IVS), papilliary muscles (PM), and left ventricle wall (LVW) are delineated in (D) the mean susceptibility map. (E) Angular difference histograms show that the MAJESTI principal eigenvectors were quite similar to DTI, especially when compared to rSTI and STI. (F) Susceptibility anisotropy maps for each reconstruction algorithm are quantitatively represented in (G) histograms of susceptibility anisotropy in the anisotropic region, *M*. (H) Sensitivity analysis showing the relationship between the median φ_1 and ν in original heart data, the data with the SNR halved, and the data with reduced spatial resolution.
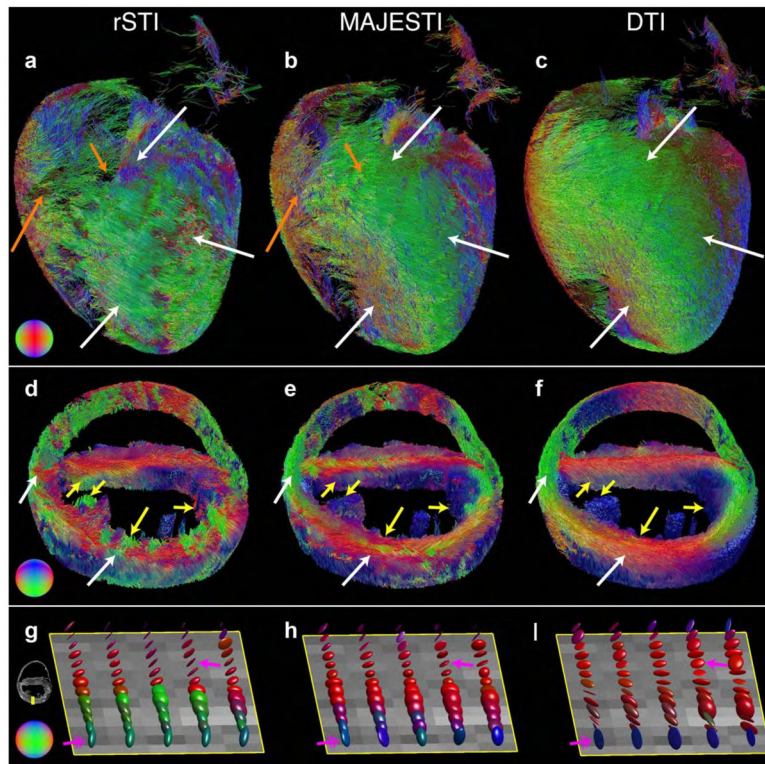
Fig. 9.
Susceptibility- and diffusion-based tractography in the mouse heart specimen. Wholeheart fiber tractography generated from (A) rSTI, (B) MAJESTI, and (C) DTI (2% of myofiber tracts longer that 0.75 mm shown). (D), (E), and (F) show 1-mm slices of the tractography data through the middle of the heart for rSTI, MAJESTI, and DTI, respectively (5% of myofiber tracts longer than 0.75 mm shown). MAJESTI exhibited fewer tractography artifacts than rSTI, as indicated by the white and yellow arrow on the outside and inside of the left ventricle, respectively. The orange arrows show regions where MAJESTI tracked fibers in the right ventricle wall that rSTI did not. Glyph plots of the (G) rSTI, (H) MAJESTI, and (I) DTI tensor data in the left ventricle wall (yellow rectangle, 0.3×1.2 mm region) show how the fiber angles transition from endocardium (top) to epicardium (bottom). The primary eigenvector direction is indicated by the glyph color, and the shape is determined by the eigenvalues. MAJESTI modestly improves the rSTI myofiber eigenvector orientations that are nearly correct without impacting the anisotropy (single pink arrows). The pink double arrows indicate where these fiber eigenvector orientation corrections were more substantial; green rSTI glyphs become purple MAJESTI glyphs, which better resembles DTI. The glyph plots were downsampled from 10×39 voxel region to 5×13 voxels in order to display the entire thickness of the LVW for each set of tensor data.

Table 1

Scan protocols for STI and DTI data acquisitions.

	Brain		Kidney		Heart	
Protocol	STI	DTI	STI	DTI	STI	DTI
Field strength (T)	7.0	7.0	9.4	9.4	9.4	9.4
Pulse sequence	MGRE	Spin echo	MGRE	Spin echo	MGRE	Spin echo
Array size	$440\times400^2\times8$	$400\times200\times220$	$256^3\times6$	256^3	$512^3\times8$	400×300^2
Isotropic resolution (µm)	50	50	55	55	30	30
Flip angle (°)	65	90/180	50	90/180	50	90/180
TR (ms)	100	100	50	100	50	100
TE_1/ TE/TE_n (ms)	4.5/6.8/52.4	14.0/–/–	3.4/2.9/17.9	11.8/–/–	3.0/5.5/41.5	15.4/–/–
Diffusion time (ms)	-	6.3	-	5.7	-	9.6
b-value (s/mm^2)	-	1,200	-	1,500	-	1,000
Number of directions	12	12	12	12	12	12
Acq. time/direction (hrs)	4.4	1.2	0.9	1.8	3.6	2.5